Applied Acoustics 217 (2024) 109816

Contents lists available at ScienceDirect

Applied Acoustics

journal homepage: www.elsevier.com/locate/apacoust

Extremely tortuous sound absorbers with labyrinthine channels in non-porous and microporous solid skeletons

Tomasz G. Zieliński [a,*], Kamil C. Opiela [a], Nicolas Dauchez [b], Thomas Boutin [b], Marie-Annick Galland [c], Keith Attenborough [d]

[a] Institute of Fundamental Technological Research, Polish Academy of Sciences, ul. Pawińskiego 5B, 02-106 Warsaw, Poland
[b] Université de Technologie de Compiègne, Alliance Sorbonne Université, Laboratoire Roberval, Centre de recherche Royallieu, CS 60319, 60203 Compiègne CEDEX, France
[c] Laboratoire de Mécanique des Fluides et d'Acoustique, Université de Lyon, École Centrale de Lyon, INSA Lyon, Université Claude Bernard Lyon I, CNRS, UMR 5509, 36 Avenue Guy de Collongue, F-69134, Ecully, France
[d] The Open University, School of Engineering and Innovation, Milton Keynes MK7 6AA, UK

ARTICLE INFO

Keywords:
Sound absorption
Extreme tortuosity
Double porosity
Acoustic composites
Additive manufacturing

ABSTRACT

An assembly of additively-manufactured modules to form two-dimensional networks of labyrinthine slits results in a sound absorber with extremely high tortuosity and thereby a relatively low-frequency quarter wavelength resonance. Fully analytical modelling is developed for the generic design of such composite acoustic panels, allowing rapid exploration of various specific designs. In addition to labyrinthine channels in a non-porous solid skeleton, a case is also considered where the skeleton has microporosity such that its permeability is very much lower than that due to the labyrinthine channels alone. The analytical modelling is verified by numerical calculations as well as sound absorption measurements performed on several 3D printed samples of modular composite panels. The experimental validation required overcoming the non-trivial difficulties related to additive manufacturing and testing samples of extreme tortuosity. However, due to the two-dimensionality and modularity of the proposed design, such absorbers can possibly be produced without 3D printing by assembling simple, identical modules produced separately. The experimental results fully confirmed the theoretical predictions that significant sound absorption, almost perfect at the peak, can be achieved at relatively low frequencies using very thin panels, especially those with double porosity.

1. Introduction

To be useful in vehicles and white goods, the sound absorbing layers deployed on surfaces should be as thin and lightweight as possible. This is rather difficult with traditional porous materials such as polymer foams or glass fibres since thick layers are required to offer absorption at low frequencies. Ideally, a useful hard-backed thin absorbing layer will offer a first absorption peak associated with its quarter wavelength resonance at a wavelength that is much larger than the layer thickness. Often this is called sub-wavelength performance. To meet the requirement of sub-wavelength performance, there has been a lot of exploration of what can be achieved through additive manufacturing. Many of the resulting designs are based on metamaterial approaches [1]. A particular structural form uses the notion of 'coiled' or 'coiled up' space based on relatively long internal channels. This strategy was used by Cai et al. [2], who studied thin acoustic panels that effectively absorb low-frequency sound due to coplanar coiled tubes and/or chambers. A recent example of such a design consists of 3D printed stackable solid plate elements, each of which contains a coplanar spiral rectangular channel open only at one end [3]. Since the channel widths are on the order of millimetres, there is visco-thermal attenuation and since they have finite lengths there is 'closed pipe' resonance also. An appropriate combination of channel lengths and cross sections is found to widen the absorption peak [3]. Similar research shows results obtained for sound absorbers composed of a perforated plate covering a coiled coplanar air chamber [4], acoustic metasurfaces composed of coiled channels and embedded apertures [5], or acoustic panels with coiled Helmholtz resonators [6] or multi-layer Helmholtz resonators with extended necks [7]. Several studies have explored composite structures with labyrinthine channels [8–11], or coiled-up cavities that resemble labyrinths, usually covered by perforated or slitted facesheets [12–14].

* Corresponding author.
E-mail address: tzielins@ippt.pan.pl (T.G. Zieliński).

https://doi.org/10.1016/j.apacoust.2023.109816
Received 5 August 2023; Received in revised form 25 November 2023; Accepted 12 December 2023
Available online 28 December 2023

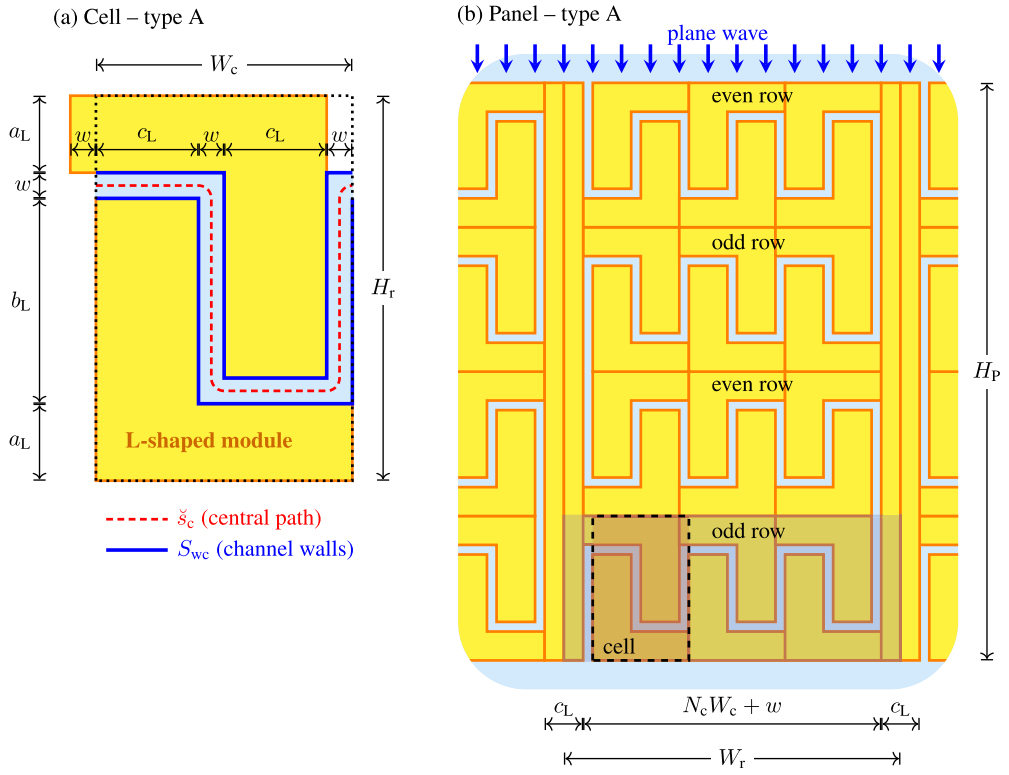

Fig. 1. Modular panel geometry – 'top' views of: (a) a representative panel cell composed of modules with L-shaped cross-sections, and (b) one panel segment. For possible panel variants, see Appendix A.

An alternative way of decreasing the quarter wavelength resonance of a hard-backed layer of porous material is to increase its tortuosity. Increasing tortuosity increases the sound path in the material thereby increasing its effective thickness and reducing the effective sound speed within it. Previously published methods of increasing tortuosity in idealised rigid porous materials include inclining straight pores, non-uniform pore cross-sections, intersecting pores, partitioning and labyrinthine perforations [15,16]. Of these, the use of labyrinthine perforations is expected to result in the largest values of tortuosity. Twisted or labyrinthine channels or perforations may be regarded as tortuous macropores in a solid or microporous matrix, if they are relatively narrow, i.e. not formed from coiled-up cavities or wide passages as in the works cited above. Thus, extreme values of tortuosity can be achieved with proper design. Moreover, an additional attenuation mechanism of pressure diffusion [17,18] can be introduced if the matrix is microporous and the micropores are much smaller than the width or cross-section of the labyrinth channels, to provide a high permeability contrast between the microporous matrix and the labyrinthine pore network. The high contrast of permeability is necessary not only for pressure diffusion to occur, but also to avoid decreasing the main pore network's extreme tortuosity by viscous leakages through the micropores. This paper describes the theoretical basis, analytical models and rigorous numerical and experimental validation of such modular acoustic materials with extremely tortuous labyrinthine channels and an impermeable or – in the second case – permeable, microporous skeleton. Note that this design is different from acoustic composites with resonant inclusions and internal structures formed by thin, impermeable, rigid walls embedded in a porous matrix, usually made of conventional acoustic foams or wools [19–26].

The outline of this paper is as follows. Section 2 presents the resizeable modular geometry of the proposed acoustic composite panels and all necessary formulae for analytical modelling of such structures with extreme tortuosity. Additive manufacturing of samples of a few prototype panels is discussed in Section 3. Numerical verification of the analytical modelling is extensively discussed in Section 4, where the theoretical predictions of sound absorption by extremely tortuous panels are also validated by the results of acoustic measurements conducted on 3D printed samples. The main findings, conclusions, and research perspectives are summarised in Section 5.

2. Theory of modular acoustic panels with high tortuosity

2.1. Resizeable modular geometry

Let us consider a composite panel composed of L-shaped modular elements. Two such elements are arranged in a (quasi) rectangular cell, as depicted in Fig. 1(a), forming a tortuous slit of width w between them. The L-shape proportions and cell dimensions are fully defined by a_L, b_L, c_L, and w, as shown in the picture, so that one side of L is equal to $a_L + b_L$ and the other side – which also defines the cell width W_c – equals $2(c_L + w)$. The cells are arranged in a row, in N_c columns inside a single panel section which in turn contains N_r rows such that for $N_r > 1$ all 'odd' rows (i.e. first, third, etc.) are identical, while each 'even' row (i.e. second, fourth, etc.) is a mirror copy of the 'odd' row. Fig. 1(b) shows the panel from above and focuses on one of its segments, where a single cell and the first odd row are highlighted. Panel segments are separated by partitions with a width c_L. Therefore, the entire width of row or section is the sum of N_c cell widths increased by the slit width and the width of the partition, i.e.

$$W_r = N_c W_c + c_L + w\,, \qquad W_c = 2c_L + 2w\,. \tag{1}$$

The panel thickness H_P is simply a multiple of the row height H_r, namely

$$H_P = N_r H_r\,, \qquad H_r = 2a_L + b_L + w\,. \tag{2}$$

The proposed geometry is resizeable and fully defined by six independent geometric parameters: four lengths, w, a_L, b_L, and c_L, and two positive integers, N_c and N_r. It is advised that the L-shape dimensions

are greater than (or equal to) the slit width w. Below we present the necessary formulae for several geometric quantities that will be used in the analytical modelling of the composite panel.

Let us first determine the total length s_r of the continuous slit channel passing through a single row in the panel section, as it will be useful for further derivations. We have

$$s_\mathrm{r} = N_\mathrm{c} s_\mathrm{c} + H_\mathrm{r}\,, \qquad s_\mathrm{c} = 2b_\mathrm{L} + 2c_\mathrm{L} + 2w\,, \tag{3}$$

where s_c is the total length of the channel inside a single cell. The above definitions describe the length of the central line of the channel when this line has sharp bends. This line should indicate the averaged flow path through the channel. We will demonstrate that for greater accuracy one should rather use curved paths that better resemble streamlines of viscous and inviscid flows through the channel. This will be evidenced by numerical simulations – see streamlines in Fig. 4(a,b) in Section 4.1 for both types of flows. Thus, let us consider the case where all the bends of the central line (but not the channel walls) are rounded with circular arcs and find the length of such a path with rounded bends across the entire row $\check{s}_\mathrm{r}$ and in a single cell $\check{s}_\mathrm{c}$. The latter is marked with a dashed red line in Fig. 1(a). To do so, the length of each sharp bend – equal to $2\frac{w}{2}$ – has to be replaced by the smaller length $\frac{\pi}{2}\frac{w}{2}$ of the corresponding quarter-circle arc. There are four bends in each cell which means that the length of the channel path inside the cell is modified by subtracting $4w$ and adding πw. Therefore, the respective expressions are

$$\check{s}_\mathrm{r} = N_\mathrm{c}\check{s}_\mathrm{c} + H_\mathrm{r}\,, \qquad \check{s}_\mathrm{c} = s_\mathrm{c} - 4w + \pi w\,. \tag{4}$$

We will also use the total length of the channel walls S_wr in the plane of a single row of the panel and the corresponding area A_rf of the fluid-saturated channel in that single row. These can be calculated from the channel length s_r as

$$S_\mathrm{wr} = 2s_\mathrm{r}\,, \qquad A_\mathrm{rf} = s_\mathrm{r} w\,. \tag{5}$$

Finally, the area of the solid part A_rs inside a single row and the total area of the row A_r are

$$A_\mathrm{rs} = A_\mathrm{r} - A_\mathrm{rf}\,, \qquad A_\mathrm{r} = W_\mathrm{r} H_\mathrm{r}\,. \tag{6}$$

2.2. Procedure and formulae for purely analytical modelling

It is assumed that the frame of the composite panel is stiff enough to allow the use of the rigid-frame models that essentially replace the acoustic composite with an equivalent fluid [27]. However, due to the additional property of the material of the frame, two kinds of panels will be considered: (1) single-porosity panels with the frame made of solid impervious material, and (2) double-porosity panels – with the microporous frame. In the latter case, it is assumed that the micropore network is open with the characteristic sizes much smaller than w, ensuring good scale separation and high permeability contrast between this network and the slit channels [28,17,29,30].

In order to predict sound absorption by a modular composite panel we need first to determine two independent, effective properties of the material, e.g. the effective density and speed of sound. It will be shown below that those are calculated on the basis of the characteristic dynamic functions related to visco-inertial and thermal effects in the tortuous slit channels, as well as to pressure diffusion in the microporous skeleton – in the latter case only for panels with double porosity. One way to calculate the dynamic functions is by using the scaling functions that depend on a set of macro-parameters (viz. tortuosity, volume fractions, characteristic lengths, static permeabilities) determined from the panel's internal geometry. In general, the macro-parameters can be calculated numerically by solving three or, in the double-porosity case, four boundary value problems defined on the appropriate representative domains [31,32,29,33,30]. However, in the case of the modular panels, they can be calculated or very accurately estimated using analytical expressions presented below.

Perhaps the most important macro-parameter of the proposed modular composites is tortuosity, because it strongly influences the viscous permeability, and the recommended modular approach allows creation of extremely tortuous panels. The tortuosity is often treated as an intrinsic parameter of a porous medium and estimated as the shortest path (or average flow path length) to the straight-line length across the porous medium [34,35]. Following Carman's original definition [36], the square of this value is often used [34], and we will analytically calculate the tortuosity of panel as

$$\alpha_\infty = (N_\mathrm{r}\check{s}_\mathrm{r}/H_\mathrm{P})^2 = (\check{s}_\mathrm{r}/H_\mathrm{r})^2\,. \tag{7}$$

We will demonstrate that this formula is very accurate when $w < \min(b_\mathrm{L}, c_\mathrm{L})$, or if $b_\mathrm{L} = 0$ then $w < N_\mathrm{c} W_\mathrm{c}$. Here, the symbol '<' practically means 'a few times larger', however, we can even have $w = b_\mathrm{L} < c_\mathrm{L}$.

The slit channels of the composite panel are saturated with a fluid, and that fluid is air. The frame is solid, although it can also be microporous. The volume fraction of the fluid is the porosity ϕ associated with the main pore network, i.e. the slit channels. The solid volume fraction ϕ_d will only be needed in the case of double porosity, referring in practice to the microporous domain. These two volume fractions are complementary, viz.

$$\phi = A_\mathrm{rf}/A_\mathrm{r}\,, \qquad \phi_\mathrm{d} = A_\mathrm{rs}/A_\mathrm{r} = 1 - \phi\,. \tag{8}$$

The characteristic lengths associated with viscous, thermal and pressure diffusion effects are

$$\Lambda_\mathrm{v} = w\,, \qquad \Lambda_\mathrm{th} = 2A_\mathrm{rf}/S_\mathrm{wr}\,, \qquad \Lambda_\mathrm{d} = 2A_\mathrm{rs}/S_\mathrm{wr}\,, \tag{9}$$

respectively. Note that here, the viscous length Λ_v is fairly accurately but nevertheless approximated with the exact result for straight slits and may slightly differ from the numerically determined value due to bends in the channel. On the contrary, the expressions for the thermal length Λ_th and the pressure diffusion length Λ_d are their formal definitions, although in a general three-dimensional case A_rf and A_rs denote the corresponding volumes and S_wr is the surface of the channel walls. Moreover, when using relations (5) one can see at once that the thermal length is in fact equal to the channel width. It is also easy to show that $\Lambda_\mathrm{d}/\phi_\mathrm{d} = \Lambda_\mathrm{th}/\phi$. Therefore,

$$\Lambda_\mathrm{v} = \Lambda_\mathrm{th} = w\,, \qquad \Lambda_\mathrm{d} = w\phi_\mathrm{d}/\phi\,. \tag{10}$$

The next required macro-parameters are the static viscous $\mathcal{K}_0$ and thermal Θ_0 permeabilities, and in the case of double porosity also the static pressure diffusion $\mathcal{B}_0$. Each of them can be related to the square of the corresponding characteristic length multiplied by the corresponding volume fraction, viz.

$$\mathcal{K}_0 = \frac{\phi\Lambda_\mathrm{v}^2}{\zeta_\mathrm{v}\,\alpha_\infty}\,, \qquad \Theta_0 = \frac{\phi\Lambda_\mathrm{th}^2}{\zeta_\mathrm{th}}\,, \qquad \mathcal{B}_0 = \frac{\phi_\mathrm{d}\Lambda_\mathrm{d}^2}{\zeta_\mathrm{d}}\,. \tag{11}$$

The values of ζ_v, ζ_th, and ζ_d can be found analytically for simple pore and solid domain geometries. In particular, $\zeta_\mathrm{v} = \zeta_\mathrm{th} = 8$ for straight cylindrical channels, and similarly, $\zeta_\mathrm{d} = 8$ for straight microporous cylinders, while $\zeta_\mathrm{v} = \zeta_\mathrm{th} = \zeta_\mathrm{d} = 12$ for straight, infinite slits and microporous partitions separating them [27,37,38]. In [39] the values of the dividing factor ζ were calculated numerically for straight rectangular perforations (in that case $\zeta_\mathrm{th} = \zeta_\mathrm{v} = \zeta$ and $\alpha_\infty = 1$) by solving dedicated Poisson problems defined on rectangular domains with successively changing proportions. The proportions can be described by the parameter ξ defined as the ratio of the side lengths of the rectangular domain. Here, we propose the analytical function

$$\zeta(\xi) = \zeta_{||} - (\zeta_{||} - \zeta_{\square})\frac{(2+\beta)\xi}{1+\beta\xi+\xi^2} = 12 - \frac{15.98\,\xi}{1+1.27\,\xi+\xi^2} \tag{12}$$

which – for the fitting parameter $\beta = 1.27$ – reproduces the numerical results presented in [39] with high accuracy, see Fig. 2. Function $\zeta(\xi)$ reaches its maximum value $\zeta_{||} = 12$ for straight, infinite slits, i.e.

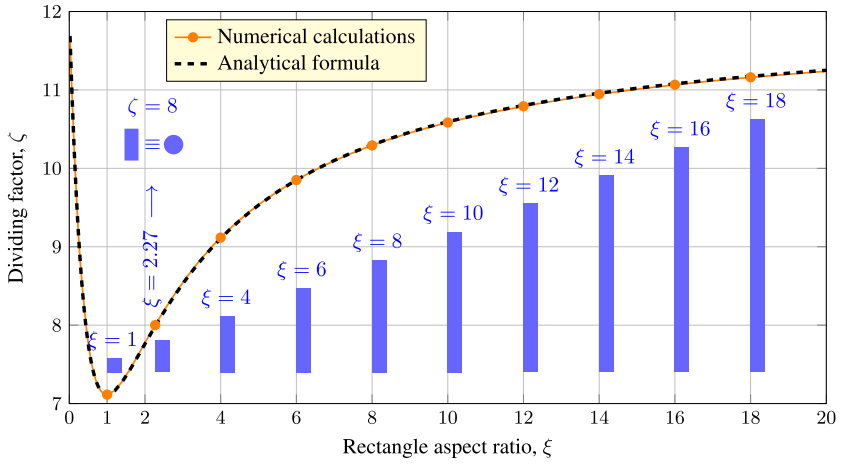

Fig. 2. The dividing factor versus the rectangle proportions: numerical calculations [39] vs. analytical formula (12).

when $\xi = 0$ or $\xi \to \infty$, while the minimum value $\zeta_{\square} = 7.114$ is obtained for square domains, i.e. when $\xi = 1$. Formula (12) will be used to estimate ζ_{d}. In practice, $\zeta_{\mathrm{d}} \approx \zeta\left((a_{\mathrm{L}} + b_{\mathrm{L}})/c_{\mathrm{L}}\right)$ can be a good estimate when b_{L} is larger than c_{L} and a_{L}. As for the viscous and thermal effects we will simply assume the upper limit, i.e. $\zeta_{\mathrm{v}} = \zeta_{\mathrm{th}} = 12$, although a slightly lower value (nearer 11) should be a better estimate as clearly seen from Fig. 2.

The macro-parameters introduced above are used to calculate characteristic frequencies and shape factors of the porous medium. The angular characteristic frequencies associated with the viscous, thermal, and pressure diffusion effects are defined as

$$\omega_{\mathrm{v}} = \frac{\phi\, \nu_{\mathrm{a}}}{\mathcal{K}_0 \alpha_\infty}, \qquad \omega_{\mathrm{th}} = \frac{\phi\, \tau_{\mathrm{a}}}{\Theta_0}, \qquad \omega_{\mathrm{d}} = \frac{\phi_{\mathrm{d}} \mathcal{D}_{0\mathrm{m}}}{\mathcal{B}_0}, \tag{13}$$

respectively. Here: $\nu_{\mathrm{a}} = \eta_{\mathrm{a}}/\varrho_{\mathrm{a}}$ is the kinematic viscosity of air, i.e. the ratio of the dynamic viscosity η_{a} to the density ϱ_{a}; $\tau_{\mathrm{a}} = \kappa_{\mathrm{a}}/(\varrho_{\mathrm{a}} C_{pa})$ is the thermal diffusivity of air, i.e. the thermal conductivity κ_{a} divided by the density ϱ_{a} and the specific heat capacity at constant pressure C_{pa}; $\mathcal{D}_{0\mathrm{m}} = \mathcal{K}_{0\mathrm{m}} P_0/(\phi_{\mathrm{m}} \eta_{\mathrm{a}})$ is the static pressure diffusivity of the microporous skeleton material related to its static viscous permeability $\mathcal{K}_{0\mathrm{m}}$ and microporosity ϕ_{m}, as well as the ambient mean pressure P_0 and dynamic viscosity of air saturating the pores and micropores. Note that the term ϕ_{m}/P_0 means the static effective compressibility of air in micropores.

The shape factors related to viscous, thermal, and pressure diffusion effects are defined as

$$\mathcal{M}_{\mathrm{v}} = \frac{8\mathcal{K}_0 \alpha_\infty}{\phi \Lambda_{\mathrm{v}}^2}, \qquad \mathcal{M}_{\mathrm{th}} = \frac{8\Theta_0}{\phi \Lambda_{\mathrm{th}}^2}, \qquad \mathcal{M}_{\mathrm{d}} = \frac{8\mathcal{B}_0}{\phi_{\mathrm{d}} \Lambda_{\mathrm{d}}^2}, \tag{14}$$

respectively. Finally, if the static viscous $\alpha_{0\mathrm{v}}$, thermal $\alpha_{0\mathrm{th}}$, and pressure diffusion $\alpha_{0\mathrm{d}}$ tortuosities are specified, e.g. by numerical calculations, the corresponding low-frequency correction factors

$$\mathcal{P}_{\mathrm{v}} = \frac{\mathcal{M}_{\mathrm{v}}}{4(\alpha_{0\mathrm{v}}/\alpha_\infty - 1)}, \qquad \mathcal{P}_{\mathrm{th}} = \frac{\mathcal{M}_{\mathrm{th}}}{4(\alpha_{0\mathrm{th}} - 1)}, \qquad \mathcal{P}_{\mathrm{d}} = \frac{\mathcal{M}_{\mathrm{d}}}{4(\alpha_{0\mathrm{d}} - 1)}, \tag{15}$$

can be calculated. These corrections will be omitted (i.e. $\mathcal{P}_{\mathrm{v}} = \mathcal{P}_{\mathrm{th}} = \mathcal{P}_{\mathrm{d}} = 1$) in fully analytical modelling.

The dynamic functions mentioned at the beginning of this section are the dynamic viscous $\mathcal{K}(\omega)$ and thermal permeability $\Theta(\omega)$, and the dynamic pressure diffusion function $\mathcal{B}(\omega)$. They can be determined as

$$\mathcal{K}(\omega) = X_\omega(\mathcal{K}_0, \mathcal{M}_{\mathrm{v}}, \mathcal{P}_{\mathrm{v}}, \omega_{\mathrm{v}}), \quad \Theta(\omega) = X_\omega(\Theta_0, \mathcal{M}_{\mathrm{th}}, \mathcal{P}_{\mathrm{th}}, \omega_{\mathrm{th}})$$
$$\mathcal{B}(\omega) = X_\omega(\mathcal{B}_0, \mathcal{M}_{\mathrm{d}}, \mathcal{P}_{\mathrm{d}}, \omega_{\mathrm{d}}), \tag{16}$$

respectively, where the scaling function

$$X_\omega(X_0, \mathcal{M}, \mathcal{P}, \omega_{\mathrm{c}}) = X_0 \left(\frac{\mathrm{i}\omega}{\omega_{\mathrm{c}}} + 1 - \mathcal{P} + \sqrt{\mathcal{P}^2 + \frac{\mathcal{M}}{2} \frac{\mathrm{i}\omega}{\omega_{\mathrm{c}}}} \right)^{-1} \tag{17}$$

is the key expression of the Johnson-Champoux-Allard-Lafarge-Pride (JCALP) model [40–43].

We can simplify the calculation procedure in fully analytical modelling. Namely, when the static permeabilities $\mathcal{K}_0$ and Θ_0, and static pressure diffusion $\mathcal{B}_0$ are determined using expressions (11), the formulae for the corresponding characteristic frequencies (13) reduce to

$$\omega_{\mathrm{v}} = \frac{\zeta_{\mathrm{v}} \nu_{\mathrm{a}}}{\Lambda_{\mathrm{v}}^2}, \qquad \omega_{\mathrm{th}} = \frac{\zeta_{\mathrm{th}} \tau_{\mathrm{a}}}{\Lambda_{\mathrm{th}}^2}, \qquad \omega_{\mathrm{d}} = \frac{\zeta_{\mathrm{d}} D_{0\mathrm{m}}}{\Lambda_{\mathrm{d}}^2}, \tag{18}$$

while those for shape factors (14) simplify to

$$\mathcal{M}_{\mathrm{v}} = 8/\zeta_{\mathrm{v}}, \qquad \mathcal{M}_{\mathrm{th}} = 8/\zeta_{\mathrm{th}}, \qquad \mathcal{M}_{\mathrm{d}} = 8/\zeta_{\mathrm{d}}. \tag{19}$$

It is now easy to see that for cylindrical pores $\mathcal{M}_{\mathrm{v}} = \mathcal{M}_{\mathrm{th}} = 1$, and similarly for cylindrical rods $\mathcal{M}_{\mathrm{d}} = 1$, which means that non-unity values of shape factors describe the deviation from the cylindrical shape. For example, all shape factors equal $\frac{2}{3}$ for straight slits. Proceeding further in this way, formulae (15) can be reduced to $\mathcal{P}_{\mathrm{v}} = (2/\zeta_{\mathrm{v}})/(\alpha_{0\mathrm{v}}/\alpha_\infty - 1)$, $\mathcal{P}_{\mathrm{th}} = (2/\zeta_{\mathrm{th}})/(\alpha_{0\mathrm{th}} - 1)$, and $\mathcal{P}_{\mathrm{d}} = (2/\zeta_{\mathrm{d}})/(\alpha_{0\mathrm{d}} - 1)$. Recall, however, that in the analytical calculations we will neglect the low-frequency corrections and assume that $\mathcal{P}_{\mathrm{v}} = \mathcal{P}_{\mathrm{th}} = \mathcal{P}_{\mathrm{d}} = \mathcal{P} = 1$. Now, the dynamic functions (16) can be expressed in terms of porosity, tortuosity, dividing factors, and characteristic lengths as follows

$$\mathcal{K}(\omega) = Y_\omega(\phi/\alpha_\infty, \zeta_{\mathrm{v}}, \Lambda_{\mathrm{v}}, \nu_{\mathrm{a}}), \quad \Theta(\omega) = Y_\omega(\phi, \zeta_{\mathrm{th}}, \Lambda_{\mathrm{th}}, \tau_{\mathrm{a}})$$
$$\mathcal{B}(\omega) = Y_\omega(1 - \phi, \zeta_{\mathrm{d}}, \Lambda_{\mathrm{d}}, \mathcal{D}_{0\mathrm{m}}), \tag{20}$$

where the scaling function

$$Y_\omega(\psi, \zeta, \Lambda, \mathcal{N}) = \psi \left(\frac{\mathrm{i}\omega}{\mathcal{N}} + \frac{\zeta}{\Lambda^2} \sqrt{1 + \frac{4\Lambda^2}{\zeta^2} \frac{\mathrm{i}\omega}{\mathcal{N}}} \right)^{-1} \tag{21}$$

is a reshaped expression of the Johnson-Champoux-Allard-Lafarge (JCAL) model which is obtained from the JCALP formula (17) for $\mathcal{P} = 1$. If we recall that $\Lambda_{\mathrm{v}} = \Lambda_{\mathrm{th}} = w$ and the dividing factors ζ_{v} and ζ_{th} can be fixed to 12 (or a slightly lower value), then the only required geometric parameters that have to be calculated in the analytical design process are ϕ and α_∞ in the case of modular composite panels with single porosity, and additionally ζ_{d} and $\Lambda_{\mathrm{d}} = w(1 - \phi)/\phi$ when the composite frame is microporous. Moreover, these parameters are determined at once from the analytical formulae given above, and then only equations (20) and a few analytical expressions given below have to be computed for quick assessment of sound absorption by the proposed composite panels, which allow for rapid analytical optimisation of such composites.

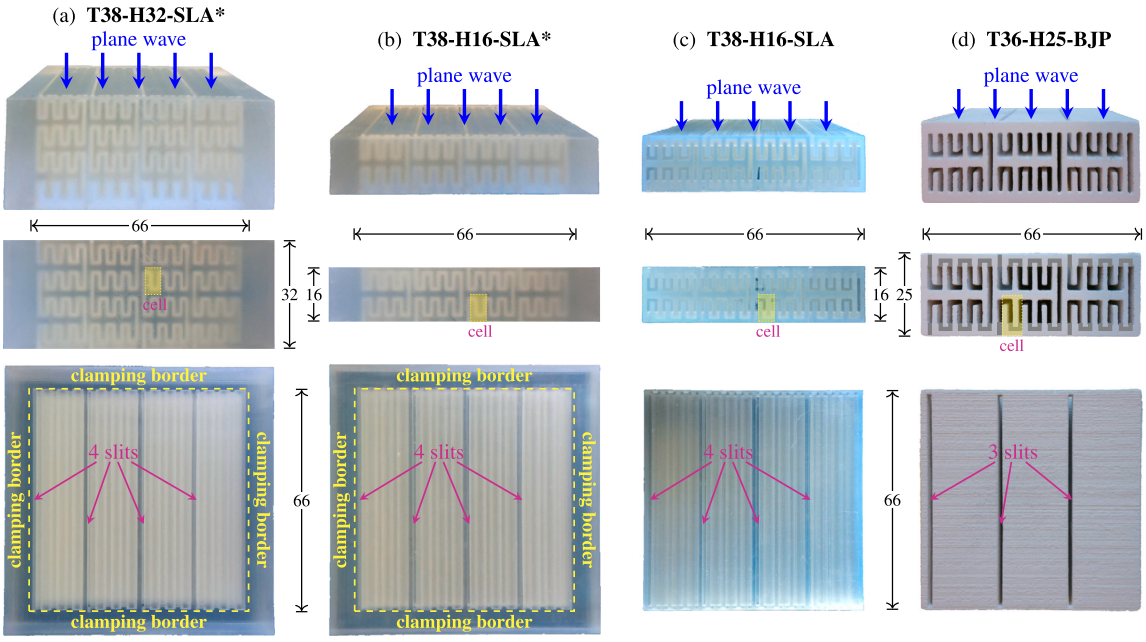

Fig. 3. Square samples of: (a) 32 mm and (b, c) 16 mm panels 3D printed in the SLA technology from a transparent resin, and (d) a 25 mm double-porosity panel 3D printed in the BJP technology from a gypsum powder (this material is not transparent, so hidden parts of the labyrinthine slits are drawn in the middle photo showing the side of this sample). Samples marked with an asterisk (*) were printed with clamping borders.

Alternatively, a model based on the exact analytical solution obtained for straight slits [27,37,38] can be used for the evaluation of viscous and thermal dynamic permeabilities. In the case of visco-inertial effects, the solution is modified by tortuosity α_∞, which is very important if the slits are oblique or tortuous. In this modelling, the dynamic functions $\mathcal{K}(\omega)$ and $\Theta(\omega)$ can be expressed in terms of porosity, tortuosity, and characteristic lengths as follows

$$\mathcal{K}(\omega) = T_\omega(\phi/\alpha_\infty, \Lambda_\mathrm{v}, \nu_\mathrm{a}), \qquad \Theta(\omega) = T_\omega(\phi, \Lambda_\mathrm{th}, \tau_\mathrm{a}), \tag{22}$$

where the function based on the exact analytical solution is

$$T_\omega(\psi, \Lambda, \mathcal{N}) = \frac{\psi\mathcal{N}}{\mathrm{i}\omega}\left(1 - \frac{\tanh\left(\frac{1}{2}\Lambda\sqrt{\mathrm{i}\omega/\mathcal{N}}\right)}{\frac{1}{2}\Lambda\sqrt{\mathrm{i}\omega/\mathcal{N}}}\right). \tag{23}$$

We have verified that $T_\omega(\psi, \Lambda, \mathcal{N}) \approx Y_\omega(\psi, 12, \Lambda, \mathcal{N})$, i.e. this model gives practically the same results as the JCAL model (21) with $\zeta_\mathrm{v} = \zeta_\mathrm{th} = 12$ which is exact for straight, parallel, infinite slits.

As already mentioned above, to determine the sound absorption of a modular panel, one first needs to calculate its effective properties. The effective compressibility of the single-porosity panel is

$$C_\mathrm{sg}(\omega) = \frac{\phi}{P_0}\left(1 - \frac{\gamma_\mathrm{a} - 1}{\gamma_\mathrm{a}}\frac{\Theta(\omega)}{\phi\,\tau_\mathrm{a}}\mathrm{i}\omega\right), \tag{24}$$

where γ_a is the heat capacity ratio for air.

In the case of double-porosity panels, the effective compressibility is calculated as

$$C_\mathrm{db}(\omega) = C_\mathrm{sg}(\omega) + \phi_\mathrm{d}\mathcal{F}_\mathrm{d}(\omega)\frac{\phi_\mathrm{m}}{P_0}, \qquad \mathcal{F}_\mathrm{d}(\omega) = 1 - \frac{\mathcal{B}(\omega)}{\phi_\mathrm{d}\mathcal{D}_\mathrm{0m}}\mathrm{i}\omega, \tag{25}$$

where the function $\mathcal{F}_\mathrm{d}(\omega)$ describes the ratio of the averaged pressure locally fluctuating in the microporous skeleton of the composite panel to the pressure in the slit channel which is locally constant. Let us also recall that ϕ_m/P_0 is the effective compressibility of air in micropores. Now, the effective density $\varrho_\mathrm{e}(\omega)$ and speed of sound $c_\mathrm{e}(\omega)$ are

$$\varrho_\mathrm{e}(\omega) = \frac{\eta_\mathrm{a}}{\mathrm{i}\omega\mathcal{K}(\omega)}, \qquad c_\mathrm{e}(\omega) = \sqrt{\frac{\mathrm{i}\omega\mathcal{K}(\omega)}{\eta_\mathrm{a}\,C(\omega)}}, \tag{26}$$

where $C(\omega) = C_\mathrm{sg}(\omega)$ for the case of single porosity, and $C(\omega) = C_\mathrm{db}(\omega)$ for the case of double porosity with high permeability contrast. The effective properties (26) allow the determination of sound propagation and absorption in the panels modelled as equivalent fluids, and in multilayer systems containing such panels.

3. Additively manufactured samples of prototype panels

Four panel samples (see Fig. 3) were additively manufactured for testing in an impedance tube with a square cross-section instead of a circular one to comply with the specific constraints of the slit network [44]. Three of these samples have the same design of slits, marked **T38** (the number refers to the designed tortuosity value), and they were 3D printed in Stereolithography (SLA) [45,46], using a low-viscosity photopolymer resin and the *Formlabs Form 3B* device. Sample **T38-H32-SLA*** is twice as thick ($H_\mathrm{P} = 32$ mm, $N_\mathrm{r} = 4$) as samples **T38-H16-SLA*** and **T38-H16-SLA** (with $H_\mathrm{P} = 16$ mm, $N_\mathrm{r} = 2$). The samples shown in Figs. 3(a) and (b) were manufactured with clamping borders in order to clamp them firmly to the end of a square impedance tube with cross-sectional dimensions 66 mm × 66 mm, or between two parts of such tube in the case of measurements with backing air gaps. Sample **T38-H16-SLA** shown in Fig. 3(c) can be inserted into the square tube, but otherwise it is identical to the **T38-H16-SLA*** sample. Panel sample **T36-H16-BJP**, depicted in Fig. 3(d), was also manufactured to fit tightly inside the tube. It was 3D printed from a coarse-grain gypsum powder in Binder Jetting 3D Printing (BJP) [47,46], using the *3D Systems ProJet 160* printer. To remove residual powder from the slits without breaking the sample, its design – marked **T36** – has much wider slits and thicker labyrinth walls than in the **T38** design. However, the tortuosity of both designs is intentionally very similar, and for this reason, the gypsum-based sample is thicker (for $N_\mathrm{r} = 2$: $H_\mathrm{P} = 25$ mm) and has three slit channels, i.e. one less than in the resin-based panel samples, cf. Figs. 3(d) and (c).

Dimensions of both slit network designs, i.e. **T38** and **T36**, are listed in Table 1. Many studies have shown that the actual dimensions of the essential details of the pore networks in additively manufactured acoustic materials deviate from the nominal values set in the designs used for 3D printing [48–50,30,51]. Therefore, design adjustments are required

Table 1
Dimensions (in millimetres) of the modular geometry: (a) the nominal values in composite panel designs, and (b) the actual values (i.e. corrected by Δw) in the samples 3D printed using the specified technologies

Design & technology		Δw	w	a_L	b_L	c_L	W_r	H_r
T38	(a) nominal	—	1.00	1.00	5.00	1.30	16.10	8.00
($N_c = 3$)	(b) **SLA**	−0.10	0.90	1.05	5.00	1.40	16.10	8.00
T36	(a) nominal	—	1.50	1.50	8.00	1.50	21.00	12.50
($N_c = 3$)	(b) **BJP**	−0.10	1.40	1.55	8.00	1.60	21.00	12.50

to improve the accuracy of predictions based on the designed geometry of the pore network. The most essential dimension in the slit networks of modular composite panels is the slit width w. It has to be updated using an estimated slit width correction Δw, which can be negative and depends on the material and technology used for manufacturing of the samples. In the case of photopolymer resin and SLA technology, the slits are slightly narrower than in the design used for 3D printing. Based on microscopic examination of the samples and the long-term experience in using the *Formlabs Form 3B* 3D printer, we can accurately estimate the slit correction in this case as $\Delta w = -0.1$ mm. The situation is not so obvious for the BJP sample, where the width of the slits varies: in most places it is narrower than the nominal design value, but it is also slightly wider in some other places, mainly due to the rather aggressive removal of powder residues from the slits. However, after careful microscopic examination, we decided that in the gypsum sample, the average slit correction could also be roughly estimated as $\Delta w = -0.1$ mm. In any case, the correction is made by the following replacement

$$w \leftarrow w + \Delta w\,, \qquad a_L \leftarrow a_L - \Delta w/2\,, \qquad c_L \leftarrow c_L - \Delta w\,. \tag{27}$$

Note that b_L, W_c, W_r, H_r, and H_P are not affected by this replacement, see equations (1) and (2). This correction and all formulae derived in the previous sections are valid provided that $-w < \Delta w < c_L$ and $\Delta w < 2a_L$. Table 1 shows the nominal and corrected dimensions of the modular geometry. The latter are related to the specific technology – SLA or BJP – used to manufacture the panel samples. These corrected values were used in the relevant calculations of the acoustic properties of these panels.

The resin samples manufactured in the SLA technology have solid, impermeable skeletons, so these are materials of single porosity formed by labyrinthine slits. The BJP sample has a similar network of labyrinthine slits, but double porosity due to the open microporosity of the gypsum skeleton made of coarse grains bound with a butyrolactam binder [30,52]. Direct measurements performed on disc-shape gypsum samples 3D printed in this technology revealed that the (micro)porosity of this material is about 40%, while permeability is about $7 \cdot 10^{-13}$ m^2, but can be slightly lower (for disks 3D printed horizontally in a powder bed) or even twice as high (for disks 3D printed in a vertical position), which shows transverse isotropy of the material with respect to the vertical direction of the layer-by-layer additive manufacturing process.

4. Numerical and experimental validation

4.1. Results for the 32 mm composite panels

First, consider the thicker 32 mm **T38** panel discussed in Section 3, see Fig. 3(a). Sound absorption by this panel backed by a rigid wall will be calculated using two approaches: (i) fully analytical modelling, and (ii) hybrid, i.e. semi-analytical, but essentially numerical, multiscale calculations based on the Multiscale Asymptotic Method [31,32,29]. In the latter case, all finite element analyses were performed using *COMSOL Multiphysics*. To accurately show the difference between single and double porosity cases – and since only a single-porosity sample of this panel was manufactured – all numerical and analytical analyses are performed for the actual dimensions of the modular geometry of the **T38-H32-SLA*** sample made of resin, see data in line '(b) SLA' for **T38** in Table 1.

In the fully analytical modelling, the dynamic functions (20) are calculated using the JCAL model (21) where the porosity ϕ, tortuosity α_∞, dividing factors $\zeta_v = \zeta_{th} = 12$ and ζ_d, as well as characteristic lengths $\Lambda_v = \Lambda_{th} = w$ and Λ_d are determined analytically or known a priori. The remaining macro-parameters (11), characteristic frequencies (13), and shape factors (14) are calculated from the relevant analytical formulae and listed in Table 2 for comparison with the corresponding numerical results obtained by the hybrid multiscale approach, as discussed below. Note that $f_v = \omega_v/(2\pi)$, $f_{th} = \omega_{th}/(2\pi)$, and $f_d = \omega_d/(2\pi)$.

In the hybrid approach, first, the macro-parameters, viz. the volume fractions ϕ and ϕ_d, kinematic α_∞ and static tortuosities α_{0v}, α_{0th}, α_{0d}, characteristic lengths Λ_v, Λ_{th}, Λ_d, and static permeabilities $\mathcal{K}_0$, Θ_0, $\mathcal{B}_0$ are calculated numerically by solving relevant boundary value problems as discussed, e.g. in [53,54,29,32,33,30], although ϕ, ϕ_d, Λ_{th} and Λ_d are determined directly from the geometry. In particular, we solve the scaled Stokes' flow, Laplace's and Poisson's problems defined in the fluid subdomain, i.e. in the channel inside a single row of the panel. For the double-porosity case, an additional Poisson's problem is solved in the subdomain of the microporous skeleton. We define and solve these problems using the finite element method, strictly adhering to all numerical requirements as discussed, e.g. in [33]. For example, the finite element mesh for the Stokes' flow has boundary layers to ensure correct determination of the high velocity gradient close to the channel walls where the no-slip boundary condition is applied. For the Laplace's problem, all sharp corners of the channel walls are filleted (with the radius of $w/20$) to avoid singularity when determining the viscous length. The antisymmetric boundary conditions are applied on the upper and lower outlet/inlet boundaries of the channel (inside the single row of the panel) in the case of Stokes' flow and Laplace's problem, while the symmetric boundary conditions in the case of the Poisson's problems. Fig. 4 shows the respective solution results, i.e. the scaled fields of: (a) viscous flow velocity projected onto the 'vertical' direction, (b) potential flow gradient projected onto the 'vertical' direction, (c) temperature in the channel, and (d) pressure variation in the skeleton. The 'vertical' direction is the direction of the external pressure gradient driving the viscous flow and consistent with the wave propagation direction. This is also the direction of the external unit vector field that induces the potential i.e. inviscid flow. Streamlines for both flows are shown in Fig. 4(a,b). The scaled potential flow gradient is dimensionless. The velocity, temperature, and pressure fields are scaled to the permeability unit (m^2), so after averaging over the considered panel fragment, they give the static viscous $\mathcal{K}_0$ and thermal Θ_0 permeabilities, and the static pressure diffusion $\mathcal{B}_0$, respectively. The tortuosity α_∞ as well as the viscous length Λ_v is calculated using the potential flow gradient. For all necessary formulae and more discussions on the subject see [33]. The numerically computed values of macro-parameters are used to analytically (hence this approach is hybrid) calculate the characteristic frequencies (13), shape factors (14), and low-frequency corrections (15), which in turn are used to determine the dynamic functions (16) using the JCALP model (17).

Table 2 compares the analytically determined parameters with the corresponding values found on the basis of numerical analyses. In gen-

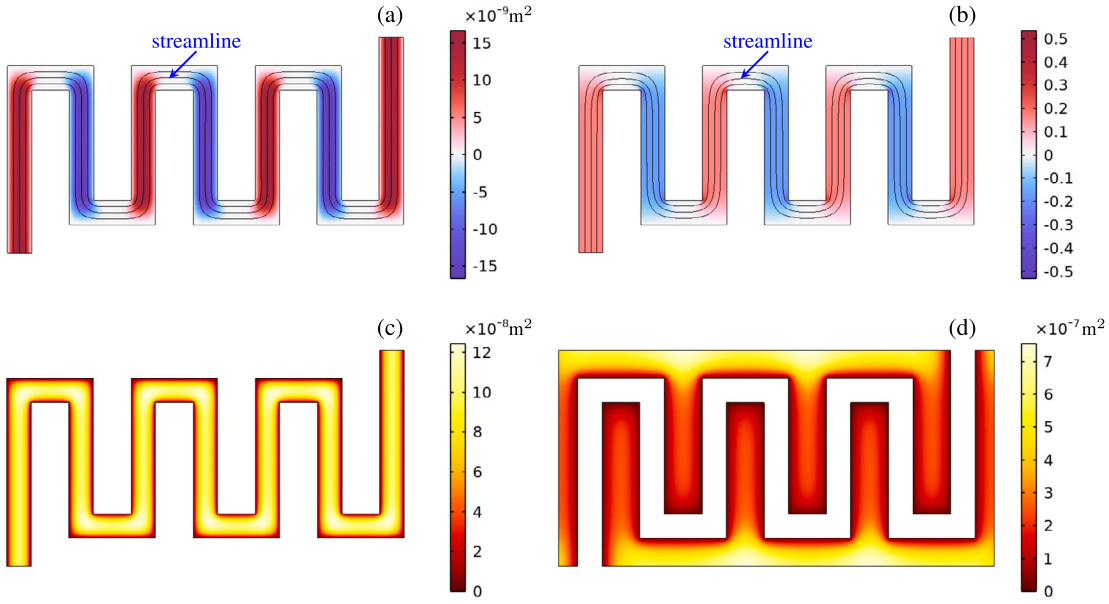

Fig. 4. Results of finite element analyses for hybrid mutliscale calculations: (a) Stokes flow, (b) Laplace problem for inviscid flow, (c) Poisson problem for static thermal diffusion, (d) Poisson problem for static pressure diffusion.

Table 2
Macro-parameters (upper table) and other related parameters (lower table) determined analytically and numerically for the **T38** panel.

type of analysis	ϕ %	ϕ_d %	α_∞ —	α_{0v} —	α_{0th} —	α_{0d} —	Λ_v mm	Λ_{th} mm	Λ_d mm	$\mathcal{K}_0$ 10^{-10}m²	Θ_0 10^{-8}m²	$\mathcal{B}_0$ 10^{-7}m²
analytical	36.20	63.80	38.26	—	—	—	0.900	0.900	1.586	6.386	2.443	1.735
numerical	36.20	63.80	37.94	46.33	1.217	1.489	0.839	0.900	1.587	6.186	2.553	1.696

type of analysis	ζ_v —	ζ_{th} —	ζ_d —	$\mathcal{M}_v$ —	$\mathcal{M}_{th}$ —	$\mathcal{M}_d$ —	$\mathcal{P}_v$ —	$\mathcal{P}_{th}$ —	$\mathcal{P}_d$ —	f_v Hz	f_{th} Hz	f_d Hz
analytical	12	12	9.26	0.667	0.667	0.864	1	1	1	37.6	53.4	5528
numerical	10.84	11.48	9.47	0.738	0.697	0.845	0.834	0.804	0.432	39.1	51.1	5657

eral, the agreement is very good. In particular, the numerical and analytical values of volume fractions ϕ and ϕ_d, and two characteristic lengths Λ_{th} and Λ_d are identical as they all represent the exact values. The analytical approximation of tortuosity (7) proves to be very accurate due to the proposed correction of quarter-circle bends, which is indicated by the streamlines of the viscous and potential flows shown in Fig. 4(a,b). The alternative tortuosity value $(s_r/H_r)^2 = 41.93$ calculated for sharp bends is evidently less accurate. The numerical value of Λ_v is almost 7% smaller than the slit channel width w adopted a priori for Λ_v in analytical calculations and exact only for straight slits. This is due the bends of the channel, which affect the viscous characteristic length. Finally, note that the numerical values of ζ_v, ζ_{th}, and ζ_d were found by inverting the expressions (11) and taking numerical values for all other parameters present in these formulae. Furthermore, only numerically calculated values are given for α_{0v}, α_{0th} and α_{0d}, since the static tortuosities are not determined by analytical calculations and are not required by the JCAL scaling function; also recall that the JCALP model reduces to the JCAL model for $\mathcal{P}_v = \mathcal{P}_{th} = \mathcal{P}_d = 1$.

Once the dynamic functions are determined using the analytical or hybrid approach, the effective compressibility can be calculated for the single-, Eq. (24), and double-porosity case, Eq. (25), and then the corresponding effective density and speed of sound (26). In the case of double porosity, the microporosity ϕ_m and static viscous permeability $\mathcal{K}_{0m}$ of the microporous skeleton (see Section 3 for their directly measured values) were first used to determine the required static pressure diffusivity $\mathcal{D}_{0m} = 9.44 \cdot 10^{-3}\ \mathrm{m}^2/\mathrm{s}$. All dynamic and effective properties as well as the characteristic frequencies and static pressure diffusivity are computed for the relevant air properties listed in Table 3. Their values were determined for the ambient mean pressure and temperature conditions found during acoustic testing of the 3D printed samples of prototype panels.

Figs. 5 and 6 compare the dynamic functions and the corresponding effective compressibilities calculated using both approaches, showing very good agreement between them. Note that the peaks in the negative imaginary parts of all these functions are located close to the respective characteristic frequencies. Pay attention in particular to the second peak on the curve of the negative imaginary part of the normalised effective compressibility for the double-porosity structure (Fig. 6). This peak is close to the characteristic frequency $f_d = \omega_d/(2\pi) = 5528\,\mathrm{Hz}$, but it drives the curve up far below this frequency, so that the values at frequencies already above 200 or 300 Hz are much greater than the values of the corresponding curve determined for the single porosity case. This means that the pressure diffusion phenomenon in the double-porosity structure should be significant already at such low frequencies.

The effective properties calculated for both 32 mm composite panels, i.e. with single- and double-porosity, allowed the prediction of sound absorption for these composites backed by a rigid wall, using the fully analytical and hybrid approaches. These predictions are shown in Fig. 7 and, consequently with the above findings, the differences between the 'Analytical' and 'Hybrid' results are barely visible in both porosity cases. There is, however, a significant difference between the sound absorption by the single-porosity panel and the double-porosity composite of the same meso-geometry of tortuous channels due to pressure diffusion in the microporous skeleton. In particular, the pronounced first

Table 3
Air properties at ambient conditions of pressure P_0 and temperature T_0.

P_0 hPa	T_0 °C	ϱ_a kg/m^3	c_a m/s	γ_a —	η_a Pa·s	κ_a W/(m·K)	C_{pa} J/(kg·K)	ν_a m^2/s	τ_a m^2/s
993.6	25.9	1.155	347.0	1.40	$1.841{\cdot}10^{-5}$	$2.631{\cdot}10^{-2}$	1006	$1.594{\cdot}10^{-5}$	$2.264{\cdot}10^{-5}$

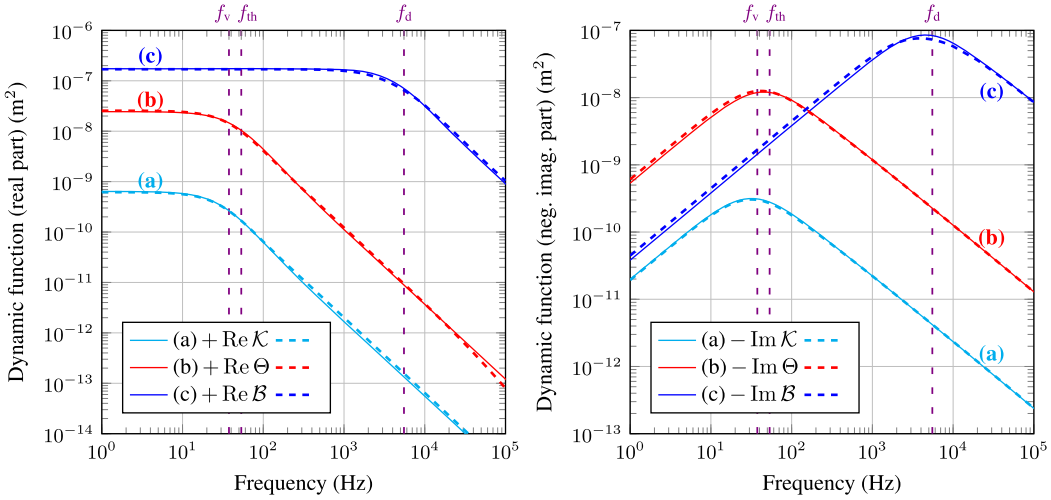

Fig. 5. Dynamic (a) viscous and (b) thermal permeabilities, and (c) pressure diffusion function, calculated analytically (continuous lines) and numerically (dashed lines) for the **T38** absorber.

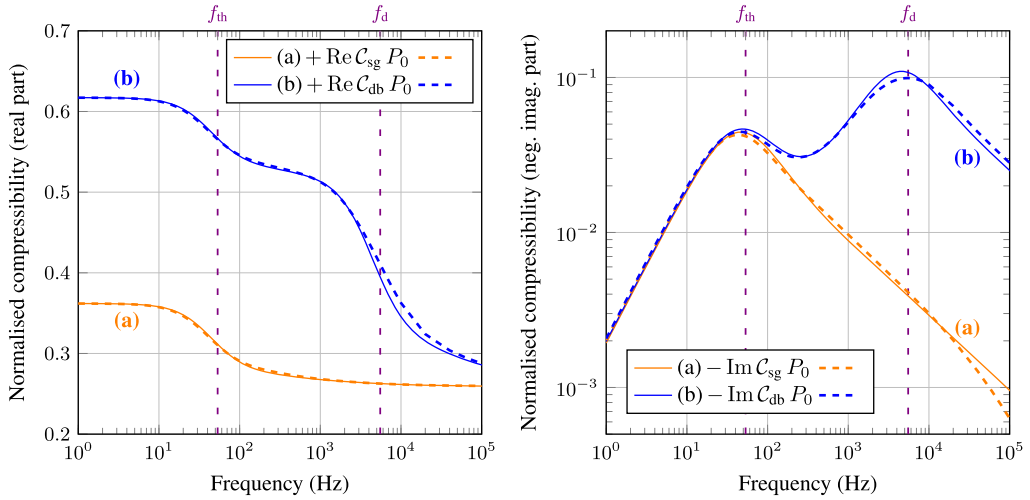

Fig. 6. Normalised effective compressibility for the **T38** absorber with (a) single or (b) double porosity, calculated analytically (continuous lines) and numerically (dashed lines).

absorption peak of approximately 0.8 at 400 Hz (single-porosity panel) is advantageously shifted to 290 Hz and slightly increased to 0.87 for the double-porosity panel, although even the first of these frequencies is already quite low (see the comment above to Fig. 6).

Due to the difficulty of removing powder residues from slits in BJP printouts, only the single-porosity SLA sample of the 32 mm panel was manufactured – see Fig. 3(a) – and tested in the impedance tube. The results of these measurements confirm the theoretical predictions for this single-porosity panel very well, especially in the target low-frequency range (see Fig. 7): some clear yet still acceptable discrepancies between the single-porosity absorption curves occur only at higher frequencies above 1.2 kHz. The double-porosity predictions shown in Fig. 7 have not been experimentally verified for this panel, but they illustrate the potential improvement, which has been fully confirmed by experimental tests on the double-porosity material with wider slits as discussed below.

4.2. Sound absorption by the 16 mm and 25 mm composite panels

Figs. 8 and 9 show sound absorption curves measured and calculated for 16 mm and 25 mm panels with designed tortuosities of approximately 38 and 36, respectively. Each figure shows two separate graphs: (a) for a composite panel directly backed by a rigid wall, and (b) for a configuration with an air gap of 5 mm between the composite and the rigid wall. Each graph shows the calculation results for the single and double porosity cases. All calculations were performed for the actual dimesnions of the 3D printed samples, see the respective 'SLA' and 'BJP' rows in Table 1. The values of macroparameters calculated for the 3D printed samples are listed in Table 4. They were determined analyt-

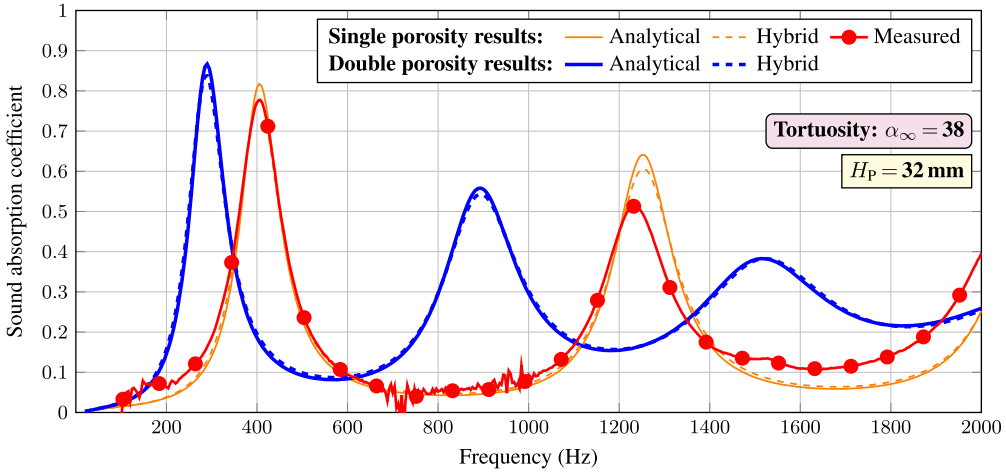

Fig. 7. Sound absorption by the **T38-H32** panels of single or double porosity.

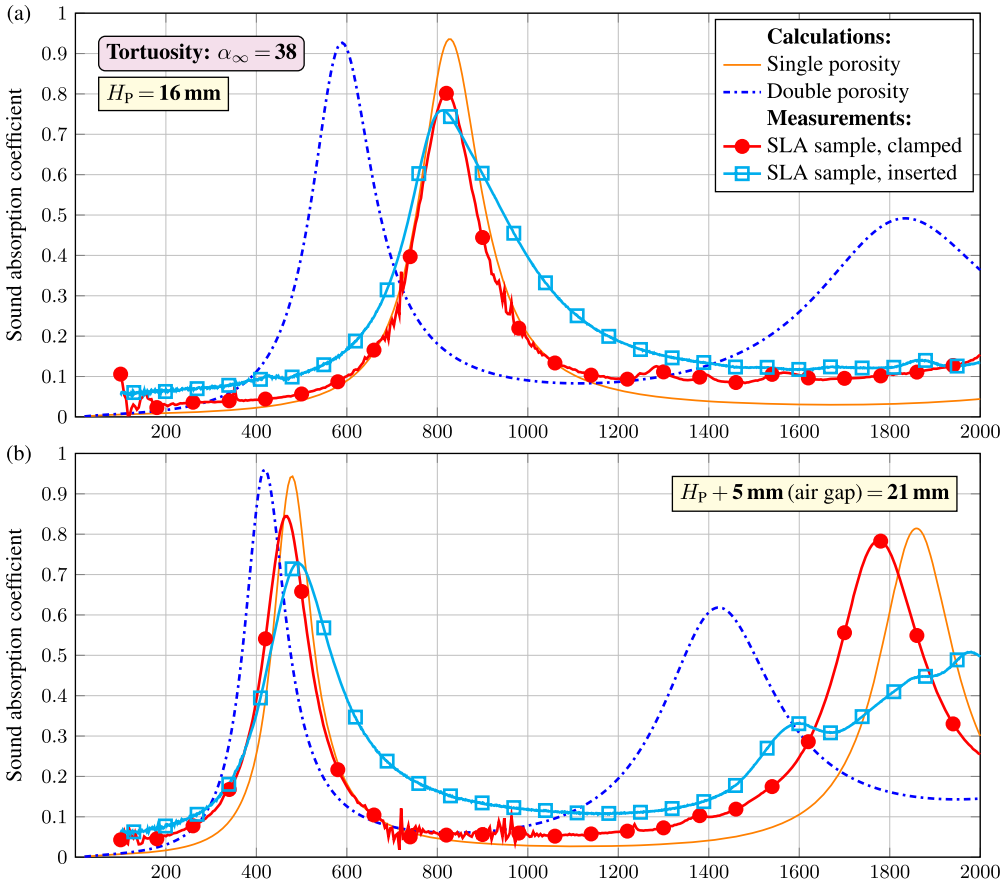

Fig. 8. Sound absorption calculated and measured for the single-porosity **T38-H16-SLA** samples: (a) with a rigid backing, or (b) backed by an air gap of 5 mm. In each graph, the absorption curves measured for the clamped and inserted samples are compared with the results predicted for single and double porosity cases.

ically – note that the values for **T38** are actually copied for convenience from the 'analytical' row of Table 2. The characteristic frequencies for the viscous f_v, thermal f_{th}, and pressure diffusion f_d effects are given in the last three columns of Table 4 and they were calculated by dividing by 2π the respective formulae (13), and assuming relevant air properties determined during the acoustic testing (see Table 3). To calculate the values of f_d, and consequently for all predictions for double-porosity composites, we used $\phi_m = 0.40$ and $\mathcal{K}_{0m} = 7 \cdot 10^{-13}$ m^2 (so $\mathcal{D}_{0m} = 9.44 \cdot 10^{-3}$ m^2/s) as determined for the microporous material made from gypsum powder in the BJP technology, see Section 3. When reading Table 4, recall that the pressure diffusion parameters and characteristic frequency f_d are only relevant for the case of double porosity.

Sound absorption curves predicted for thin panels with networks of extremely tortuous slits have rather specific nature. They are characterised by a peak of perfect or near-perfect absorption at relatively low frequency. For the hard-backed panels with single porosity, this frequency is close to 800 Hz for the **T38** panel with $\alpha_\infty = 38$ and $H_P = 16$ mm, see Fig. 8(a), and it is 550 Hz for the **T36** panel with $\alpha_\infty = 36$ and $H_P = 25$ mm, see Fig. 9(a). This is consistent with the well-known fact that by increasing the tortuosity, the sound absorption efficiency can be shifted to a lower frequency range. Achieving

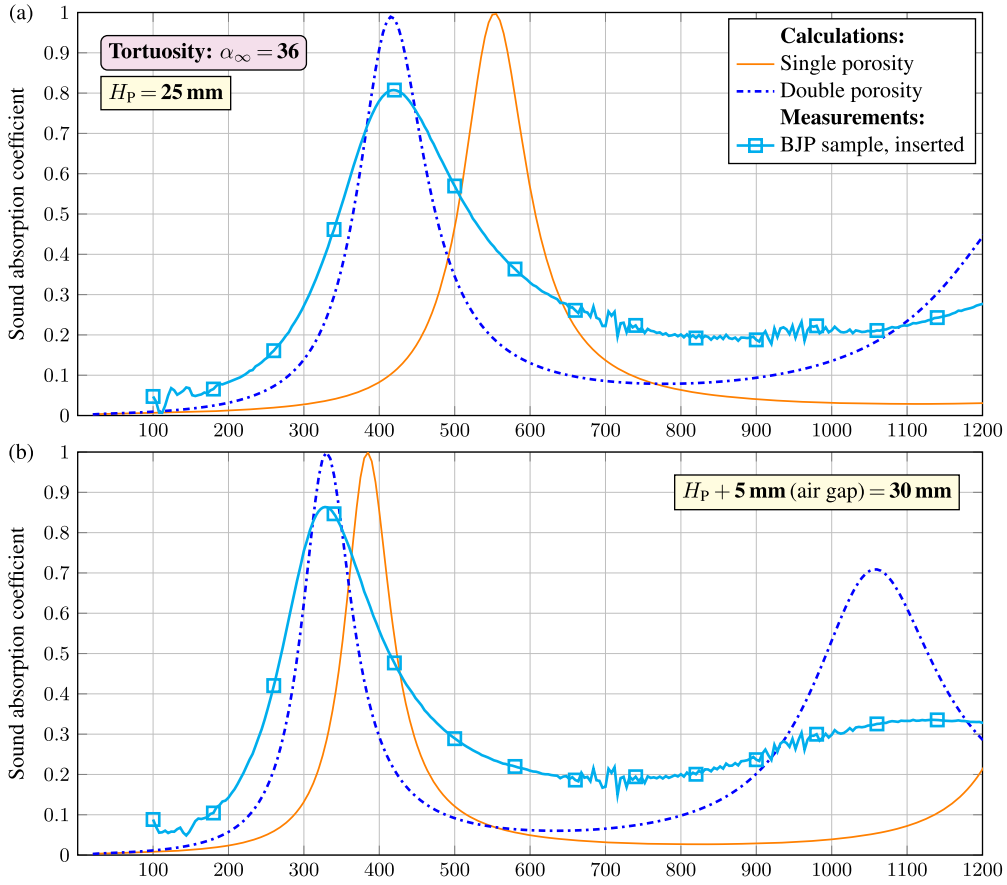

Fig. 9. Sound absorption calculated and measured for the double-porosity **T36-H25-BJP** sample: (a) with a rigid backing, or (b) backed by an air gap of 5 mm. Each graph shows predictions for single and double porosity cases.

Table 4
Macro-parameters and characteristic frequencies determined for the designed panels with slit network tortuosities equal to approximately 38 and 36. Pressure diffusion parameters and characteristic frequency f_d are relevant only for the case of double porosity.

Panel	visco-thermal effects					pressure diffusion				charact. frequencies		
	ϕ %	α_∞ —	$\Lambda_v = \Lambda_{th}$ mm	$\mathcal{K}_0$ 10^{-10}m^2	Θ_0 10^{-8}m^2	ϕ_d %	ζ_d —	Λ_d mm	$\mathcal{B}_0$ 10^{-7}m^2	f_v Hz	f_{th} Hz	f_d Hz
T38	36.20	38.26	0.900	6.386	2.443	63.80	9.26	1.586	1.735	37.6	53.4	5528
T36	41.87	35.90	1.400	19.05	6.838	58.13	9.84	1.944	2.232	15.5	22.1	3915

near-perfect absorption at low frequencies using such thin layers can be considered an achievement. However, the sound absorption is not broadband but rather localised in the frequency range around the peak. This is mainly due to the low porosity of the single-porosity panels (about 36% or 42% – see the values of ϕ in Table 4). This situation can be improved by the use of a microporous material for the skeleton of the composite panels to obtain double-porosity structures with well-contrasted permeabilities ensuring pressure diffusion. In this case, the absorption peaks are still high but shifted towards much lower frequencies, namely below 600 Hz in the case of the **T38** panel, and to almost 400 Hz for the **T36** panel. Significant sound absorption is still located around the peak, but the frequency range of relatively good absorption can even be conceptually widened, if we note that the range of a few hundred hertz can be considered locally wide when it is located well below 1 kHz, and when the aim is to absorb mainly low-frequency sound. For example, the sound absorption coefficient of the designed 16 mm panel with double porosity is larger than 0.4 in relatively wide low-frequency range, from about 500 Hz up to 700 Hz (i.e. 200 Hz span) with the maximum of 0.93 at 590 Hz, see Fig. 8(a). Panels with such good low-frequency sound absorption properties can be very useful as this is not achievable with conventional acoustic materials, when we recall that the thickness is only 16 mm.

Experimental validation of the proposed concept turned out to be more difficult than expected, in particular due to problems with removing powder residues from extremely tortuous, labyrinthine pore networks, but also due to measurement issues. For this reason, all measurements were performed in two square impedance tubes independently in two different laboratories to guard against errors resulting from the difficulty of testing materials with such extreme tortuosities. The tests used the well-known two-microphone transfer function method in accordance with the ISO standard [55]. In this article, we present results in the frequency range up to 2 kHz, which is well below the frequency limit of 2.6 kHz established for impedance tubes with a 66 mm square cross-section. Initially the absorption curves measured for the samples inserted into the tube differed significantly from the predictions, in particular the absorption peak appeared at a higher frequency. We realised that this was due to sound leakages around the sample edges. This is a well-known effect that should be avoided even when measuring conventional porous materials in a circular impedance tube, which is achieved by properly fitting and, if necessary, sealing the

sample [56,55]. However, in the case of the tested samples, the sealing had to be particularly tight, because even a very small leak around an extremely tortuous sample can be critical to the accuracy of the measurements, as the edge gaps are in the form of rough but straight slits that have a tortuosity close to unity, which spoils the designed high tortuosity of the labyrinthine slits. We confirmed this by successively improving the fit and sealing, and re-measuring the absorption, which eventually agreed with the prediction. Finally, we also manufactured the samples with clamping edges – see Fig. 3(a, b) – and fastened them tightly to the square impedance tube. With these samples, the leakage problem was gone and the absorption curves matched their predictions very well. On both graphs in Fig. 8 we show the absorption curves measured for the inserted and clamped single-porosity samples 3D printed from photopolymer resin. The results for the clamped samples were easy to reproduce and in general agree very well with the predictions. The sound absorption curves measured for the inserted samples differ slightly from these results, however, we checked that the discrepancies decreased after improving the sealing.

We were unable to effectively remove powder residue from narrow slits of the **T38** labyrinthine network, so only modelling predictions of the sound absorption by such composite panels with double porosity are presented, see dash-dotted curves in Fig. 8. Instead, we manufactured a gypsum sample with not optimal but wider slits and thicker walls, see Fig. 3(d), but similarly high tortuosity (panel **T36**). The sound absorption curves measured for this 25 mm sample are confronted with the modelling predictions in Fig. 9. The comparison confirms the expectations regarding the double porosity effect: when it is taken into account in the modelling, the first absorption peak is shifted to 420 Hz, which is in perfect agreement with the first peak of the measured absorption. The measurement and modelling results obtained for the sample backed by an air gap are also affirmative. However, the discrepancies between the predictions and measurements are evident. They can be attributed to larger shape and surface imperfections of this 3D printed sample, partly also to the highly probable inhomogeneities and anisotropy of the microporous skeleton, but mainly to small sound leaks around the BJP sample as it was inserted into the impedance tube rather than clamped to it. In fact, the nature of these discrepancies is evidently the same as in the case of the inserted SLA samples. Another reason for the observed discrepancies – in the case of all samples – can be large distances between the entries to labyrinthine slits, which are 16.1 mm for the **T38** panels, and 21 mm in the case of the **T36** design. This may have some effect on wave propagation and therefore measurements at higher frequencies, as these values are only four (**T38**) or three (**T36**) times smaller than 66 mm, which is the size of the square impedance tube used for testing these composite panel samples.

5. Conclusions

The proposed sound absorbers have relatively simple, modular, and essentially two-dimensional geometry of labyrinthine slits, which provides extreme tortuosity. Modelling of such acoustic composite panels can be performed analytically, which allows for quick optimisation and examination of various specific designs. This is possible because the generic slit network consists of identical narrow channels, enabling accurate, analytical estimation of tortuosity, in which the channel length plays a key role. We have shown that this length should be corrected by taking instead the channel centreline with rounded bends, which approximates the average flow path through the channel very well. Then, the geometric estimation of tortuosity becomes very close to the actual flow-based tortuosity, which is especially important when the channels are wider.

The correctness of the applied analytical modelling was verified by numerical calculations as well as sound absorption measurements performed on several 3D printed samples of modular panels. The experimental validation required overcoming the non-trivial difficulties related to manufacturing and testing samples of extreme tortuosity: laborious removal of powder and resin residues as well as extremely tight sealing of sound leaks around the samples to avoid reduction of tortuosity. Experimental results confirmed the predicted acoustic performance of the proposed high-tortuosity structures, proving that significant sound absorption, almost perfect at the peak, can be achieved at relatively low frequencies using very thin panels. The peak frequency can even be easily lowered by making the skeleton microporous and permeable with a permeability suitably contrasted with that of the labyrinthine pore network. The effect of an air gap behind the panel – presented in this work – suggests double-layer solutions in the form of a thin, extremely tortuous panel backed by an even thinner layer of conventional acoustic material. The two-dimensionality and modularity of the proposed generic design mean that the panles can be manufactured using more conventional methods instead of 3D printing technologies used for this study. The fact that the panels can be assembled from identical modules with an L-shaped cross-section should facilitate mass production of large-surface layers.

CRediT authorship contribution statement

Tomasz G. Zieliński: Conceptualization, Formal analysis, Investigation, Methodology, Software, Visualization, Writing – original draft, Writing – review & editing. **Kamil C. Opiela:** Investigation. **Nicolas Dauchez:** Investigation, Writing – review & editing. **Thomas Boutin:** Investigation. **Marie-Annick Galland:** Investigation, Writing – review & editing. **Keith Attenborough:** Conceptualization, Validation, Writing – review & editing.

Declaration of competing interest

The authors declare that they have no known competing financial interests or personal relationships that could have appeared to influence the work reported in this paper.

Data availability

The raw data required to reproduce these findings can be obtained by contacting the corresponding author.

Acknowledgements

This research was financially supported by the National Science Centre (NCN), Poland, as part of the project “Sound-absorbing composites: coupled acoustic energy dissipation mechanisms, multiscale modelling and prototyping”, under Grant Agreement No. 2021/41/B/ST8/04492. For the purpose of Open Access, the authors have applied a CC-BY public copyright licence to any Author Accepted Manuscript (AAM) version arising from this submission.

Appendix A. Panel variants

Fig. A.1 shows alternative panel setups. These variants can be modelled as the panel from Fig. 1, after modifying just a few formulae. For Panel B, see Fig. A.1(a,b), there is no distinction between odd and even rows, but a horizontal slit of width w is added at the bottom of each row. As a consequence, the cell (row) height is increased by the slit width, i.e. $H_\mathrm{r} = 2a_\mathrm{L} + b_\mathrm{L} + 2w$, and the total length of the slit channels inside the cell is $s_\mathrm{c} = 2b_\mathrm{L} + 4c_\mathrm{L} + 4w$. There are also two additional bends in each row, therefore $\check{s}_\mathrm{r} = N_\mathrm{c}\check{s}_\mathrm{c} + H_\mathrm{r} - 2w + \pi w/2$, but all other formulae remain unchanged. Finally, panel variants with $b_\mathrm{L} = 0$ can also be modelled (note that then $w \ll N_\mathrm{c}W_\mathrm{c}$). In that case there are no bends inside the cell, see Fig. A.1(c,d), and then: $\check{s}_\mathrm{c} = W_\mathrm{c}$ and $\check{s}_\mathrm{r} = N_\mathrm{c}W_\mathrm{c} + H_\mathrm{r} - 2w + \pi w/2$ for Panel A with $b_\mathrm{L} = 0$, and $\check{s}_\mathrm{c} = 2W_\mathrm{c}$ and $\check{s}_\mathrm{r} = 2N_\mathrm{c}W_\mathrm{c} + H_\mathrm{r} - 4w + \pi w$ for Panel B with $b_\mathrm{L} = 0$. In these special cases, reasonable estimates for ζ_d are as follows: $\zeta_\mathrm{d} \approx \zeta\left(N_\mathrm{c}W_\mathrm{c}/a_\mathrm{L}\right)$ for Panel A with $b_\mathrm{L} = 0$ and $N_\mathrm{r} > 1$, and $\zeta_\mathrm{d} \approx \zeta\left(N_\mathrm{c}W_\mathrm{c}/(2a_\mathrm{L})\right)$ for Panel B with $b_\mathrm{L} = 0$ or Panel A with $b_\mathrm{L} = 0$ and $N_\mathrm{r} = 1$.

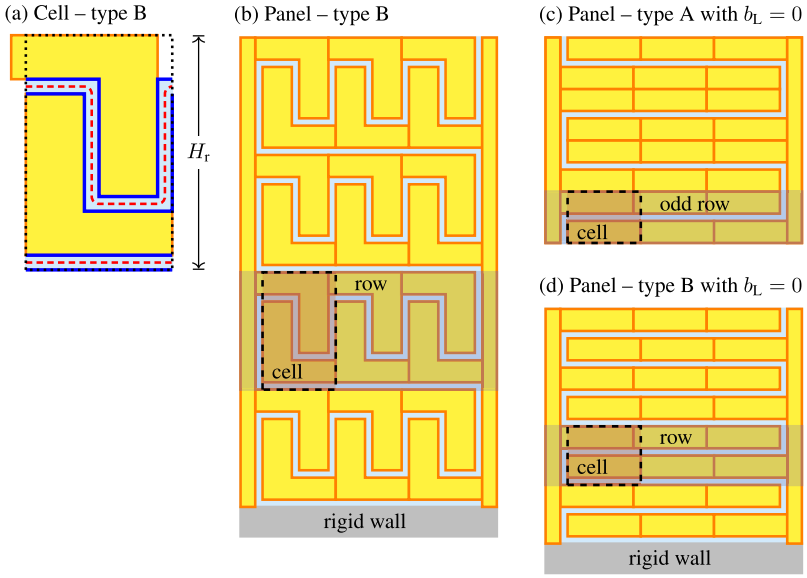

Fig. A.1. Panel variants.

References

[1] Groby J-P, Jiménez N, Romero-García V. Acoustic metamaterial absorbers. Cham: Springer International Publishing; 2021. p. 167–204.

[2] Cai X, Guo Q, Hu G, Yang J. Ultrathin low frequency sound absorbing panels based on coplanar spiral tubes or coplanar Helmholtz resonators. Appl Phys Lett 2014;105:121901. https://doi.org/10.1063/1.4895617.

[3] Prasetiyo I, Anwar K, Brahmana F, Sakagami K. Development of stackable subwavelength sound absorber based on coiled-up system. Appl Acoust 2022;195:108842. https://doi.org/10.1016/j.apacoust.2022.108842.

[4] Li Y, Assouar BM. Acoustic metasurface-based perfect absorber with deep subwavelength thickness. Appl Phys Lett 2016;108:063502. https://doi.org/10.1063/1.4941338.

[5] Huang S, Fang X, Wang X, Assouar B, Cheng Q, Li Y. Acoustic perfect absorbers via spiral metasurfaces with embedded apertures. Appl Phys Lett 2018;113:233501. https://doi.org/10.1063/1.5063289.

[6] Chen J-S, Chen Y-B, Cheng Y-H, Chou L-C. A sound absorption panel containing coiled Helmholtz resonators. Phys Lett A 2020;384:126887. https://doi.org/10.1016/j.physleta.2020.126887.

[7] Guo J, Zhang X, Fang Y, Jiang Z. Wideband low-frequency sound absorption by inhomogeneous multi-layer resonators with extended necks. Compos Struct 2021;260:113538. https://doi.org/10.1016/j.compstruct.2020.113538.

[8] Donda K, Zhu Y, Fan S-W, Cao L, Li Y, Assouar B. Extreme low-frequency ultrathin acoustic absorbing metasurface. Appl Phys Lett 2019;115:173506. https://doi.org/10.1063/1.5122704.

[9] Zhao H, Wang Y, Yu D, Yang H, Zhong J, Wu F, et al. A double porosity material for low frequency sound absorption. Compos Struct 2020;239:111978. https://doi.org/10.1016/j.compstruct.2020.111978.

[10] Kumar S, Lee HP. Labyrinthine acoustic metastructures enabling broadband sound absorption and ventilation. Appl Phys Lett 2020;116:134103. https://doi.org/10.1063/5.0004520.

[11] Yuan T, Song X, Xu J, Pan B, Sui D, Xiao H, et al. Tunable acoustic composite metasurface based porous material for broadband sound absorption. Compos Struct 2022;298:116014. https://doi.org/10.1016/j.compstruct.2022.116014.

[12] Wang Y, Zhao H, Yang H, Zhong J, Zhao D, Lu Z, et al. A tunable sound-absorbing metamaterial based on coiled-up space. J Appl Phys 2018;123:185109. https://doi.org/10.1063/1.5026022.

[13] Rui Liu C, Hui Wu J, Yang Z, Ma F. Ultra-broadband acoustic absorption of a thin microperforated panel metamaterial with multi-order resonance. Compos Struct 2020;246:112366. https://doi.org/10.1016/j.compstruct.2020.112366.

[14] Almeida GdN, Vergara EF, Barbosa LR, Brum R. Low-frequency sound absorption of a metamaterial with symmetrical-coiled-up spaces. Appl Acoust 2021;172:107593. https://doi.org/10.1016/j.apacoust.2020.107593.

[15] Attenborough K. Macro- and micro-structure designs for porous sound absorbers. Appl Acoust 2019;145:349–57. https://doi.org/10.1016/j.apacoust.2018.10.018.

[16] Attenborough K. Analytical approximations for sub wavelength sound absorption by porous layers with labyrinthine slit perforations. Appl Sci 2021;11(8):3299. https://doi.org/10.3390/app11083299.

[17] Olny X, Boutin C. Acoustic wave propagation in double porosity media. J Acoust Soc Am 2003;114(1):73–89. https://doi.org/10.1121/1.1534607.

[18] Venegas R, Boutin C. Acoustics of permeable heterogeneous materials with local non-equilibrium pressure states. J Sound Vib 2018;418:221–39. https://doi.org/10.1016/j.jsv.2017.11.013.

[19] Groby J-P, Wirgin A, De Ryck L, Lauriks W, Gilbert RP, Xu YS. Acoustic response of a rigid-frame porous medium plate with a periodic set of inclusions. J Acoust Soc Am 2009;126(2):685–93. https://doi.org/10.1121/1.3158936.

[20] Lagarrigue C, Groby JP, Tournat V, Dazel O, Umnova O. Absorption of sound by porous layers with embedded periodic arrays of resonant inclusions. J Acoust Soc Am 2013;134(6):4670–80. https://doi.org/10.1121/1.4824843.

[21] Yang J, Lee JS, Kim YY. Metaporous layer to overcome the thickness constraint for broadband sound absorption. J Appl Phys 2015;117:174903. https://doi.org/10.1063/1.4919844.

[22] Groby J-P, Huang W, Lardeau A, Aurégan Y. The use of slow waves to design simple sound absorbing materials. J Appl Phys 2015;117(12):124903. https://doi.org/10.1063/1.4915115.

[23] Groby J-P, Lagarrigue C, Brouard B, Dazel O, Tournat V, Nennig B. Enhancing the absorption properties of acoustic porous plates by periodically embedding Helmholtz resonators. J Acoust Soc Am 2015;137(1):273–80. https://doi.org/10.1121/1.4904534.

[24] Fang Y, Zhang X, Zhou J, Guo J, Huang X. Acoustic metaporous layer with composite structures for perfect and quasi-omnidirectional sound absorption. Compos Struct 2019;223:110948. https://doi.org/10.1016/j.compstruct.2019.110948.

[25] Prasetiyo I, Sihar I, Brahmana Gunawan F. Enhancing nonwoven fabric material sound absorption using embedded labyrinthine rigid structures. Appl Acoust 2022;195:108852. https://doi.org/10.1016/j.apacoust.2022.108852.

[26] Ren S, Liu Y, Sun W, Wang H, Lei Y, Wang H, et al. Broadband low-frequency sound absorbing metastructures composed of impedance matching coiled-up cavity and porous materials. Appl Acoust 2022;200:109061. https://doi.org/10.1016/j.apacoust.2022.109061.

[27] Allard JF, Atalla N. Propagation of sound in porous media: modeling sound absorbing materials. 2nd ed. Chichester: John Wiley & Sons; 2009.

[28] Boutin C, Royer P, Auriault J. Acoustic absorption of porous surfacing with dual porosity. Int J Solids Struct 1998;35(34):4709–37. https://doi.org/10.1016/S0020-7683(98)00091-2.

[29] Auriault J-L, Boutin C, Geindreau C. Homogenization of coupled phenomena in heterogenous media. John Wiley & Sons, Ltd; 2009.

[30] Zieliński TG, Dauchez N, Boutin T, Leturia M, Wilkinson A, Chevillotte F, et al. Taking advantage of a 3D printing imperfection in the development of sound-absorbing materials. Appl Acoust 2022;197:108941. https://doi.org/10.1016/j.apacoust.2022.108941.

[31] Bensoussan A, Lions J-L, Papanicolaou G. Asymptotic analysis for periodic structures. North-Holland Publishing Company; 1978.

[32] Sanchez-Palencia E. Non-homogeneous media and vibration theory. Springer-Verlag; 1980.

[33] Zieliński TG, Venegas R, Perrot C, Červenka M, Chevillotte F, Attenborough K. Benchmarks for microstructure-based modelling of sound absorbing rigid-frame porous media. J Sound Vib 2020;483:115441. https://doi.org/10.1016/j.jsv.2020.115441.

[34] Ghanbarian B, Hunt AG, Ewing RP, Sahimi M. Tortuosity in porous media: a critical review. Soil Sci Soc Am J 2013;77:1461–77. https://doi.org/10.2136/sssaj2012.0435.

[35] Sobieski W. An efficient method of tortuosity estimation. Arch Mech 2022;74:39–64. https://doi.org/10.24423/aom.3861.
[36] Carman PC. Fluid flow through granular beds. Trans Inst Chem Eng (London) 1937;15:150–66. https://doi.org/10.1016/S0263-8762(97)80003-2. reprinted in: Chem Eng Res Des 1997;75(Suppl.):S32–48.
[37] Stinson MR. The propagation of plane sound waves in narrow and wide circular tubes, and generalization to uniform tubes of arbitrary crosssectional shape. J Acoust Soc Am 1991;89(2):550–8. https://doi.org/10.1121/1.400379.
[38] Stinson MR, Champoux Y. Propagation of sound and the assignment of shape factors in model porous materials having simple pore geometries. J Acoust Soc Am 1991;91(2):685–95. https://doi.org/10.1121/1.402530.
[39] Zieliński TG, Chevillotte F, Deckers E. Sound absorption of plates with micro-slits backed with air cavities: analytical estimations, numerical calculations and experimental validations. Appl Acoust 2019;146:261–79. https://doi.org/10.1016/j.apacoust.2018.11.026.
[40] Johnson DL, Koplik J, Dashen R. Theory of dynamic permeability and tortuosity in fluid-saturated porous media. J Fluid Mech 1987;176:379–402. https://doi.org/10.1017/S0022112087000727.
[41] Champoux Y, Allard J-F. Dynamic tortuosity and bulk modulus in air-saturated porous media. J Appl Phys 1991;70:1975–9. https://doi.org/10.1063/1.349482.
[42] Lafarge D, Lemarinier P, Allard JF, Tarnow V. Dynamic compressibility of air in porous structures at audible frequencies. J Acoust Soc Am 1997;102(4):1995–2006. https://doi.org/10.1121/1.419690.
[43] Pride SR, Morgan FD, Gangi AF. Drag forces of porous-medium acoustics. Phys Rev B 1993;47(9):4964–78. https://doi.org/10.1103/PhysRevB.47.4964.
[44] Opiela K, Zieliński T, Attenborough K. Limitations on validating slitted sound absorber designs through budget additive manufacturing. Mater Des 2022;218:110703. https://doi.org/10.1016/j.matdes.2022.110703.
[45] Zhang F, Zhu L, Li Z, Wang S, Shi J, Tang W, et al. The recent development of vat photopolymerization: a review. Addit Manuf 2021;48:102423. https://doi.org/10.1016/j.addma.2021.102423.
[46] Gibson I, Rosen D, Stucker B. Additive manufacturing technologies: 3D printing, rapid prototyping, and direct digital manufacturing. 2nd edition. New York: Springer; 2015.
[47] Mostafaei A, Elliott AM, Barnes JE, Li F, Tan W, Cramer CL, et al. Binder jet 3D printing—process parameters, materials, properties, modeling, and challenges. Prog Mater Sci 2021;119:100707. https://doi.org/10.1016/j.pmatsci.2020.100707.
[48] Kennedy J, Flanagan L, Dowling L, Bennett GJ, Rice H, Trimble D. The influence of additive manufacturing processes on the performance of a periodic acoustic metamaterial. Int J Polym Sci 2019;2019:7029143. https://doi.org/10.1155/2019/7029143.
[49] Boulvert J, Costa-Baptista J, Cavalieri T, Perna M, Fotsing ER, Romero-García V, et al. Acoustic modeling of micro-lattices obtained by additive manufacturing. Appl Acoust 2020;164:107244. https://doi.org/10.1016/j.apacoust.2020.107244.
[50] Opiela KC, Zieliński TG. Microstructural design, manufacturing and modelling of an adaptable porous composite sound absorber. Composites, Part B, Eng 2020;187:107833. https://doi.org/10.1016/j.compositesb.2020.107833.
[51] Boulvert J, Gabard G, Romero-García V, Groby J-P. Compact resonant systems for perfect and broadband sound absorption in wide waveguides in transmission problems. Sci Rep 2022;12:10013. https://doi.org/10.1038/s41598-022-13944-1.
[52] Zieliński TG, Dauchez N, Boutin T, Chevillotte F, Bécot F-X, Venegas R. 3D printed axisymmetric sound absorber with double porosity. In: Desmet W, Pluymers B, Moens D, Neeckx S, editors. Proceedings of ISMA2022 international conference on noise and vibration engineering and USD2022 international conference on uncertainty in structural dynamics; 2022. p. 462–76.
[53] Gasser S, Paun F, Bréchet Y. Absorptive properties of rigid porous media: application to face centered cubic sphere packing. J Acoust Soc Am 2005;117(4):2090–9. https://doi.org/10.1121/1.1863052.
[54] Perrot C, Chevillotte F, Panneton R. Bottom-up approach for microstructure optimization of sound absorbing materials. J Acoust Soc Am 2008;124(2):940–8. https://doi.org/10.1121/1.2945115.
[55] ISO 10534-2: Determination of sound absorption coefficient and impedance in impedance tubes. 1998.
[56] Cummings A. Impedance tube measurements on porous media: the effects of airgaps around the sample. J Sound Vib 1991;151:63–75. https://doi.org/10.1016/0022-460X(91)90652-Z.